SUPPORTING INFORMATION:

Pervasive Tertiary Structure in the Dengue Virus RNA Genome

Elizabeth A. Dethoff[a,1], Mark A. Boerneke[a,1], Nandan S. Gokhale[b], Brejnev M. Muhire[c], Darren P. Martin[c], Matthew T. Sacco[b], Michael J. McFadden[b], Jules A. Weinstein[d], William B. Messer[d,2], Stacy M. Horner[b,2] and Kevin M. Weeks[a,2]

[a] Department of Chemistry, University of North Carolina, Chapel Hill, NC 27599

[b] Department of Molecular Genetics and Microbiology, Duke University Medical Center, Durham, NC 27710

[c] Institute of Infectious Disease and Molecular Medicine, University of Cape Town, 7000 Cape Town, South Africa

[d] Department of Molecular Microbiology and Immunology, Oregon Health & Science University, Portland, OR 97239

[1] These authors contributed equally to this work.

[2] correspondence: weeks@unc.edu, stacy.horner@duke.edu and messer@ohsu.edu

Supporting Text

Choice of regions targeted for structural and functional analysis and 3D modeling

We evaluated all regions with significant RING correlations for their appropriateness for structural and functional analysis and for 3D modeling by imposing four requirements: (*i*) elements should be in low SHAPE/low entropy regions consistent with forming well-determined secondary structures (Fig. 1 and SI Appendix, Fig. S1); (*ii*) elements should exhibit a high density of RING correlations consistent with true through-space interactions (SI Appendix, Figs. S5 and S6); (*iii*) elements should fold into highly similar structures in both the ex virion and refolded states; and (*iv*) observed RINGs should not extend significantly outside the low SHAPE/low entropy regions used to define each element. Regions with significant RINGs occurred in or significantly overlapped with many of the 24 elements with low SHAPE/low Shannon entropy. Of the 24 well-determined elements, elements 3, 4, 5, 8, 10, 11, 23 and 24 contained dense groups of RING correlations (Fig. 2). Of these, elements 3 and 5 fold

significantly differently in the ex virion and refolded RNA structures, and many of the RINGs in elements 11 and 23 extend to regions outside of the core element. Four elements – 4 (Env), 8 (NS2A), 10 (NS2B) and 24 (3'-UTR) – therefore met the criteria for forming well-determined 3D folds and were further studied in this work. We also modeled element 1 (5'-UTR) that has only a few RING correlations, but passes the other filters and contains a well-validated pseudoknot (1) that constrains its conformational space. Modeling (and mutational) studies on the four selected elements were performed using SHAPE-directed minimum free energy (MFE) models from the refolded RNA state (Fig. 2A, secondary structure black and gray arcs), the state for which RING-MaP data was collected. While SHAPE-directed MFE models for these four elements are highly similar for refolded and ex virion (secondary structure black arcs: Fig. 1 and SI Appendix, Fig. S1, panel 1) states, there are minor predicted differences in a few internal base pairs and small helices (Fig. 2A, secondary structure gray arcs). Importantly, SHAPE reactivity data from both the refolded and ex virion RNA states are highly correlated and minor differences in MFE structures are captured by overlapping probability arcs that summarize the underlying base-pairing probabilities, suggesting multiple conformations may be sampled in these short regions (base pair probability, green and blue arcs: Fig. 1 and SI Appendix, Fig. S1, panel 1). We also emphasize that the remaining RING-containing regions across the DENV RNA genome not selected for further study in this work remain structurally interesting and merit follow up studies.

Methods

DENV2 virions and RNA genomes

DENV2 viral particles (strain S16803, GenBank GU289914, Microbix Biosystems) were purified from tissue culture supernatants of infected Vero cells (African green monkey kidney cells) by size fractionation and sucrose density gradient centrifugation. Virions were concentrated by ultracentrifugation and resuspended in Medium 199 (pH 7.2) supplemented with Hank's salts and glutamine (10.98 g/L). For ex virion experiments, RNA was gently extracted from the virus avoiding heating, metal ion chelation, ethanol precipitation, and other potentially denaturing steps (2–4). Virions were lysed with 1.5% (w/v) SDS and 150 µg/mL proteinase K, and incubated at 37 °C for 30 min; RNA was extracted twice with 4 volumes of phenol/chloroform/isoamyl alcohol (25:24:1) pre-equilibrated with lysis buffer [50 mM HEPES (pH 8.0), 200 mM NaCl, and 3 mM $MgCl_2$], followed by two extractions with chloroform. RNA was exchanged into SHAPE-MaP buffer [50 mM HEPES (pH 8.0), 200 mM potassium acetate (pH 8.0), and 3 mM $MgCl_2$] using a size exclusion column (NAP5, GE Healthcare). For in virion

experiments, virions were exchanged into SHAPE-MaP buffer (Amicon Ultra-15 Ultracel-100, Millipore) before modification by SHAPE reagent.

SHAPE-MaP RNA structure probing

Extracted RNA or intact viruses were incubated at 37 °C in SHAPE-MaP buffer for 30 min. RNA was modified with 1-methyl-7-nitroisatoic anhydride (1M7), 1-methyl-6-nitroisatoic anhydride (1M6), or N-methylisatoic anhydride (NMIA) in individual experiments (5, 6). Briefly, RNA was added to 0.1 volume of 100 mM SHAPE reagent in DMSO (10 mM final concentration after dilution) and incubated for 4 min (1M6 and 1M7) or 22 min (NMIA). No-reagent and denaturing control (DC) control experiments (5) were performed in parallel. After modification, in virion RNA samples were extracted as described above and then all RNA samples were purified (RNeasy MinElute, Qiagen). In total, there were 11 samples: ex virion 1M7, 1M6, NMIA, and no-reagent control; in virion 1M7, 1M6, NMIA, and no-reagent control; and denaturing controls DC-1M7, DC-1M6, and DC-NMIA.

SHAPE-MaP DNA library preparation

After RNA modification and purification, MaP cDNA synthesis was performed as described (5). Briefly, RNA was fragmented by heating at 94 °C for 4 min in fragmentation buffer [150 mM Tris-HCl (pH 8.3), 9 mM $MgCl_2$, and 225 mM KCl]. Approximately 250 ng of purified, fragmented RNA (~73 fmol) was subjected to reverse transcription (Superscript II; Invitrogen) in a buffer containing 0.7 mM dNTPs, 50 mM Tris-HCl (pH 8.0), 75 mM KCl, 6 mM $MnCl_2$, and 14 mM DTT. The reaction was primed using 200 ng of random 9-mer primers and incubated at 42 °C for 3 h. To make double-stranded DNA libraries, purified cDNA was added to a second-strand synthesis reaction (NEB E6111), and end repair was performed (Enzymatics, Y9140-HC-L). Samples were dA-tailed (NEB E6053S) and ligated to Illumina-compatible TruSeq adaptors (NEB M2200L). Emulsion PCR (7) was performed (Q5 high-fidelity polymerase; NEB M0493). Samples were size-selected (Ampure XP beads; Agencourt), DNA libraries quantified (Qubit; Life Technologies), and visualized by length (Bioanalyzer; Agilent). All ex virion and in virion libraries were sequenced on a HiSeq 2500 instrument (Illumina).

SHAPE-MaP data processing

ShapeMapper (5, 8) was used to analyze all sequencing data. Raw sequencing FASTQ files were aligned to a reference DENV2 sequence and SHAPE reactivities were generated using the following parameters: minPhred = 10, minLength = 25, mapping quality = 30, minPhredToCount

= 20. SHAPE reactivities for nucleotides with a read depth of less than 2500 or with a high no-reagent mutation rate (>0.03) were excluded from analysis. Median read depths of the three ex virion and in virion samples (1M7, DMSO, and DC) were all greater than 50,000. We obtained 1M7 SHAPE reactivities for 99% of the nucleotides in the DENV2 genome in both the ex virion and in virion conditions. Full biological replicates of ex virion and in virion SHAPE-MaP experiments were performed and yielded Pearson correlation coefficients of 0.89 and 0.69, respectively.

Secondary structure modeling

ShapeKnots (implemented in RNAStructure v5.6) (9) was used to identify pseudoknots in the DENV2 genome; ex virion 1M7 reactivities were used as constraints. The genome was folded in 600-nucleotide sliding windows incremented by 100 nucleotides with the following parameters (9): slope = 1.8, intercept = -0.6, P1 = 0.35, P2 = 0.65. Extra calculations were performed on the 5' and 3' ends to increase coverage of these regions. A pseudoknot was considered plausible if (*i*) the pseudoknot was observed in a majority of folding windows that spanned the pseudoknotted helix and (*ii*) nucleotides predicted to be involved in the pseudoknotted helix had low SHAPE reactivities.

The program *SuperFold* (5, 8) based on RNAStructure *Partition* (v5.6) and both 1M7 and differential SHAPE reactivities (using 1M6 and NMIA data) (6) was used to calculate a global partition function (10, 11), which yields base-pairing probabilities for all possible canonical base pairs. *Partition* was run in 1200-nucleotide sliding windows, incremented by 100 nucleotides. Two extra partition function calculations were performed on the 5' and 3' ends of the genome to increase coverage of the ends and to reduce end effects (5, 8). The maximum base-pairing distance was set to 500 nucleotides. Pseudoknotted nucleotides were forced to be single-stranded in these calculations; therefore, base-pairing probabilities for pseudoknotted nucleotides were not calculated. Base pairs with probabilities less than 10^{-4} were ignored in further calculations. Base-pair probabilities from the multiple partition function windows were combined. Shannon entropies (12) were calculated from base-pairing probabilities from the individual partition function windows and combined into a single profile. *SuperFold* was used to incorporate 1M7 and differential SHAPE reactivities into RNAStructure *Fold* (v5.6) to generate a MFE structure (11). The most probable base pairs (probability >99%) identified by the partition function calculation were forced to be base paired. *Fold* was run with using 4000-nucleotide sliding windows incremented by 375 nucleotides. The multiple folds were combined into a final

MFE structure by requiring that accepted base pairs appeared in more than half of the windowed folds. Finally, the pseudoknotted base pairs were added to the structure. The local median SHAPE reactivity and Shannon entropy were calculated over centered sliding 55-nucleotide windows. Regions of at least 40 nucleotides with both median SHAPE reactivities and median Shannon entropies below the global medians were identified. Some regions bisected structures such that only half of a helix was included. The corresponding low entropy/low SHAPE regions were expanded or combined to include the entirety of the intersecting helices based on the MFE structure.

Ex virion and in virion SHAPE differences

Statistically significant differences between ex virion and in virion 1M7 SHAPE reactivities were detected using both Z-factor and standard-score significance criteria using the deltaSHAPE approach (13). The significance threshold was set to $|S| \geq 1$, equivalent to requiring that an individual SHAPE difference was at least one standard deviation away from the mean SHAPE difference value. Finally, within each five-nucleotide window, at least three nucleotides were required to have $Z > 0$ and an absolute standard score ≥ 1 to be considered significant. The absolute values of significant SHAPE differences were summed over a 51-nucleotide window. The global median and standard deviation were 2.78 and 2.75, respectively. Clusters of significant SHAPE differences were identified by finding continuous stretches of nucleotides with a summed difference value greater than the global median plus one standard deviation (5.5). The minimum length of this region was required to be at least 40 nucleotides.

RING-MaP

Refolded RNA was modified with dimethyl sulfate (DMS) as described (14). In brief, extracted RNA was resuspended in $0.5\times$ TE buffer [5 mM Tris (pH 7.5), 0.5 mM EDTA], heated at 85 °C for 5 min, and cooled on ice for 5 min. Then, $2.5\times$ RING-MaP buffer [final concentration 300 mM cacodylate (pH 7.0) and 10 mM $MgCl_2$] was added, and samples were incubated at 37 °C for 30 min. RNA was added to 0.1 volume of 1.7 M DMS in neat ethanol (170 mM final concentration) and incubated for 6 min. A no-reagent control was prepared in parallel using neat ethanol instead of DMS. Reactions were quenched with an equal volume of 2-mercaptoethanol and placed on ice for 5 min. Reactions were precipitated with ethanol, washed with cold 70% ethanol, and resuspended in water. To facilitate RING probing of a single MFE state, deproteinized RNA was heated and refolded before DMS modification. A small number of regions folded differently when the RNA was subjected to refolding treatment; our analysis

focuses on regions that fold the same under both ex virion and refolded RNA conditions.

Most RING-MaP data were obtained using a randomly primed reverse transcription reaction (15) that included 600 ng RNA (175 fmol) and 500 ng of random 9-mer primer. The cDNA was added to a second-strand synthesis reaction and prepared for sequencing (Nextera XT, Illumina). DNA libraries were sequenced using a NextSeq (Illumina) instrument, using paired 2×151 nucleotide sequencing reads. We were therefore able to detect through-space RINGs separated by roughly 280 nucleotides in the linear sequence. FASTQ files were aligned to the entire DENV2 sequence. The 5' and 3'-UTR regions were analyzed using a region-specific primer approach (5, 8). DENV2 RNA was modified by DMS as described above. The region-specific primer RT reactions included 250 ng RNA (73 fmol) and 2 pmol of each primer. DNA libraries were prepared using PCR. The gene-specific PCR primers for the 5'-UTR were 5'-AGTTG TTAGT CTACG TGGAC CG-3' and 5'-CTTCA ATATC CCTGC TGTTG G-3'. Those for the 3'-UTR were 5'-GCCAT CCATG AAAAG ATTTA GAAG-3' and 5'-CGTTC TGTGC CTGGA ATGAT-3'. In addition, we used region-specific primers to examine six regions of the DENV2 RNA with significant RINGs, as identified by the whole-genome approach. We confirmed that the patterns of secondary and tertiary structure RINGs were highly similar in each case. DNA libraries were sequenced on a MiSeq (Illumina) instrument. FASTQ files were aligned to the 5' and 3'-UTR sequences. ShapeMapper (5, 8) was used to process all RING-MaP sequencing data. Nucleotides with high apparent mutation rates in the no-reagent control samples (>0.03) were ignored in subsequent analyses.

Analysis of RING-MaP data

RING-induced mutations were analyzed using custom software (14) updated to allow for analysis of experiments performed by random priming and without the requirement that the location of tertiary structures be known in advance (15), using the following parameters: phred_cutoff = 20, min_distance = 10. To detect DMS mutation interdependencies, the Yates' corrected version of the Pearson's χ^2 test (16) was carried out on all possible pairs of nucleotides (14). If $\chi^2 \geq 20$ ($P < 0.00001$), the two nucleotides were taken to have a statistically significant mutation correlation. The strength and sign of the correlation was quantified by the Pearson's correlation coefficient (ρ). The standard deviation (SD) of the correlation coefficient was estimated by a heuristic approach (15). The expected number of coincident mutations for two nucleotides was calculated assuming they were not correlated. Only statistically significant correlations ($\chi^2 \geq 20$) with ($|\rho| - $ SD) ≥ 0.025 and a predicted coincidence >20 were considered

in further analysis.

Separating RINGs into secondary versus tertiary structure interactions

The contact distance between the two nucleotides of every RING was calculated using the SHAPE-directed secondary structure model of the refolded RNA without pseudoknots. To identify regions with RINGs-supported higher-order tertiary structures, RINGs with a contact distance less than 20 were first removed as these likely reflect secondary structure; the number of RINGs that a nucleotide participated in were then counted. These values were summed over a 101-nucleotide window and positions with a value greater than 16.6 (median + 1 standard deviation) were taken to have a significant degree of tertiary structure (highlighted yellow boxes: Fig. 2 and SI Appendix, Fig. S6).

Disruption of tertiary structure by LNA binding

Extracted DENV2 RNA (0.16 pmol) and LNA oligo (1.6 pmol) were mixed and heated at 85 °C for 5 min and cooled on ice for 5 min. Two LNA oligos were used in this study. LNA-PK1 is complementary to half of the 3'-DB pseudoknot, whereas the LNA-Control was designed to bind a sequence in the protein-coding region. A no-LNA control was prepared in parallel. RNA was modified with DMS or subjected to a no-reagent control as outlined above. After precipitation, all samples were subjected to affinity purification (RNeasy MinElute column, Qiagen) to remove the LNA oligo. The reverse transcription reaction was carried out using gene-specific primers. DNA libraries were prepared for sequencing using PCR, and libraries were sequenced and processed as described above.

RING-MaP-directed tertiary structure modeling

Tertiary structure models were generated using pairwise RINGs as constraints in discrete molecular dynamics (DMD) simulations. We used a coarse-grained RNA model wherein each nucleotide was modeled as three pseudo-atoms representing the phosphate, sugar, and base moieties (17–19). Two types of constraints were used: (*i*) base pairs from the SHAPE-informed secondary structure model of refolded DENV2 RNA and (*ii*) correlated nucleotide pairs determined by RING-MaP analysis. RINGs from the randomly primed RING-MaP experiment were used for modeling structures with the exception of the 5'-UTR and 3'-UTR models, which used RINGs obtained from experiments with gene-specific primers. Only statistically significant RINGs involving A and/or C nucleotides were considered. RINGs between two nucleotides ≤11 nucleotides apart in primary sequence were excluded. If $|n_i - m_i| + |n_j - m_j| \leq 11$ (where n_i and n_j

are the two correlated nucleotides and m_i and m_j are any base pair in the SHAPE-directed secondary structure model of refolded DENV2 RNA), the RING was assumed to reflect a secondary structure contact and was excluded.

DMD simulations incorporated replica exchange (20) with eight replicas run in parallel at varying temperatures. Simulations were performed using a previously validated approach (14) with modifications as follows: (*i*) simulations were run for 1 million steps using only base pairs as constraints to ensure that the secondary structure formed correctly and (*ii*) the final simulations that included RING restraints were run for 2 million steps to ensure that the relatively large DENV2 RNA structures sampled structural space sufficiently. Square-well energy potentials were used to approximate pairwise interactions, such as base pairing and stacking, electrostatic repulsion, and hydrophobic interactions (17). A free-energy bonus, dependent on the through-space distance between the sugar atoms of two RING-MaP correlated nucleotides, was applied.

DMD simulations were performed in two steps. First, only base pairs (including pseudoknots) were applied as constraints during a 1-million-step simulation. The 250 structures with the lowest free energies were selected, and a representative structure was used as the starting structure for a 2-million-step DMD simulation in which RING constraints were applied in addition to base-pair constraints. Control simulations were performed omitting RING constraints. Structural snapshots from each replica were generated every 1000 time units. Structures were filtered by radius of gyration to identify constraint-dependent collapsed structures (14). Of these structures, the 250 models with the lowest free-energies were selected and subjected to distance-based hierarchical clustering (14, 18) using OC (21). Clustering was performed such that the maximum RMSD between any two models in a given cluster was less than the predicted average RMSD, calculated based on RNA length (22). Clustering of every modeled region (except the 5'-UTR and envelope-coding region) resulted in either a single cluster of 250 structures or two clusters in which the major cluster contained >60% of the structures. The ten models from each cluster with the lowest free-energy were aligned using Theseus (23), and structure images were composed using Pymol (24).

DENV2 sequence dataset
All publically available, clinically-derived, near full-length genome DENV2 sequences (downloaded June 2012) were obtained from GenBank and aligned with MAFFT using default settings (25). This alignment was used to construct a 300-sequence dataset representative of

DENV2 genetic diversity. For synonymous substitution rate analyses, a derivative dataset was created in which sequences in this alignment were specifically aligned by codon. Although ~300 genetically distinct DENV2 full-length genomes were available for analysis, the average genetic distance between the sequences was only 0.066 (on average, 6.6 sites per 100 nucleotides differ). Therefore, while the presence of evolutionary signals in our analyses are strong evidence of selection favoring the maintenance of nucleotide sites or nucleotide-pair interactions, the absence of such signals does not imply the absence of a selective process.

Neutrality test

RNA structural elements that increase viral fitness are preserved selectively; thus, nucleotide substitutions should be more strongly disfavored at base-paired nucleotides than at unpaired nucleotides. For the 24 regions identified with low SHAPE reactivity and low Shannon entropy, we used a permutation test (26) to determine whether, at polymorphic genome sites, minor allele frequencies at base-paired sites were significantly lower than those at unpaired sites. For a particular region, Tajima's D statistic was calculated from the DENV2 alignment considering only the nucleotides modeled to be base paired. Given the number of nucleotides used to calculate this base-paired D score (BPD), unpaired D scores (UPDs) were determined for 100 equally sized datasets. UPD scores were constructed by randomly selecting (with replacement) unpaired nucleotides from the alignment. The probability that base-paired nucleotides did not display lower minor allele frequencies than unpaired sites was calculated as equivalent to the proportion of times the BPD score was lower than the 100 calculated UPD scores.

Synonymous substitution rates

Sequences corresponding to the DENV2 open reading frame were extracted from the sequence alignment. Each codon was categorized as being either a base-paired or an unpaired codon depending on whether the third position nucleotide was paired in the ex virion secondary structure model. Synonymous substitution rates at individual codon sites were estimated using the phylogenetic-based parametric maximum likelihood FUBAR method (27). For each of the 22 regions in the protein-coding region (elements 2-23), a Mann-Whitney U test was used to determine whether base-paired codons had significantly lower synonymous substitution rates than unpaired codons.

Complementarily coevolution

We used a phylogenetic-based parametric maximum likelihood complementary coevolution

detection strategy to detect evidence of coevolution between base-paired nucleotides (54). For each pair of nucleotides, we compared the standard independent sites 4×4 HKY85 nucleotide substitution model (28) to a 16×16 Muse-Modified HKY85 coevolution model (M95) (29) to determine which better described the evolution of individual nucleotide pairs. Entries in the M95 substitution matrix that represented mutations that maintained base pairing through canonical or G-U interactions were multiplied by a pairing factor λ. Entries that represented mutations that disrupted base pairing were multiplied by 1/λ. A maximum likelihood ratio test was used to determine whether specific nucleotide pairs had co-evolved. For a particular base pair, a λ > 1 and Muse 95 versus HKY85 likelihood ratio test p-value <0.05 was accepted as evidence of coevolution. Due to the computational requirements of this approach, only polymorphic pairs of nucleotides within 200 nucleotides of one another were analyzed in the input alignment. For each individual structural element, the association for all possible polymorphic nucleotide pairs between (*i*) base-pairing and non-base-pairing and (*ii*) between complementarily-coevolving and not-complementarily-coevolving was tested with a 2×2 two-tailed chi-square test. We note that previous computational survey of evolutionarily conserved secondary structure motifs across all four dengue serotypes predicted only one conserved motif outside of the 5' and 3' ends of the genome; this motif is located in the NS3-coding region and shares common base pairs with the 3' end of structural element 10 (30).

Design of higher-order RNA structure-disrupting DENV mutants
Mutations disrupting many of the predicted base-paired helices and individual nucleotides involved in RINGs (SI Appendix, Fig. S7), while maintaining the amino acid sequence and avoiding rare codons, were introduced in elements 4 (Env^{mut}), 8 (NS2A^{mut}),10 (NS2B^{mut}) and the control (element 20; NS5^{mut}). All mutant sequences maintain a codon frequency distribution (percentage of low frequency codon usage based on a human host organism) below 10% and are similar to wild-type sequences (Rare Codon Analysis Tool, GenScript). The varying number of synonymous point mutations between elements reflects the varying number and size of helices and nucleotides involved in RINGs in each element.

A second round of more focused mutants (Env^{mut2} and NS2A^{mut2}) were designed to test the functional role of nucleotides specifically predicted to be involved in tertiary contacts in the Env and NS2A RNA elements (SI Appendix, Fig. S10). For the NS2A element, all nucleotides involved in RING correlations and available for synonymous mutation were mutated. This amounted to 14 mutations, which also disrupt 10 predicted base pairs. For the Env element,

these criteria for round two mutations yielded very few nucleotides available for synonymous mutation. Hence, the criteria was relaxed to include nucleotides up to two positions away from or base paired to any nucleotide with two or more RINGs. This mutant contained 18 synonymous point mutations, which also disrupt 12 base pairs.

Dynamic light scattering experiments

Non-capped in vitro transcribed DENV2 RNA (10 µg) was heat-denatured in 0.5× TE buffer at 85 °C for 5 min and refolded by snap cooling on ice for 5 min. RNA was diluted to 120 µL for a final concentration of 10 mM $MgCl_2$ and 300 mM sodium cacodylate (pH 7.4), incubated for 30 min at 37 °C to promote tertiary folding, and then snap cooled on ice. RNA was centrifuged at 10,000×g for 1 min at room temperature, and 100 µL RNA was removed from the top (leaving the bottom 20 µL) and dispensed into a microplate well. Dynamic light scattering was measured at 22 °C using a DynaPro Dynamic Light Scattering Plate Reader with default settings, and the instrument software was used to calculate hydrodynamic radii.

DENV2 replication assays

Replication experiments were performed using p16681-T7G, which is based on the DENV2 infectious clone p16681 (31) but modified to include a 5' guanosine nucleotide at the T7 transcription start site to increase in vitro transcription efficiency. The Env^{mut}, Env^{mut2}, NS2^{mut}, NS2^{mut2}, NS2B^{mut}, and NS5^{mut} mutants were constructed in this context (BioBasic or IDT gBlocks). The Pol$^-$ plasmid contained the catalytic-lethal D663N and D664N mutations in p16681-T7G. RNAs were transcribed from XbaI-linearized plasmids (MEGAscript T7 Transcription kit, Thermo-Fisher), purified by phenol-chloroform extraction, and capped with m7G (Vaccinia capping system, NEB). RNAs were visualized by denaturing formaldehyde gel electrophoresis before use to ensure quality. BHK-21 cells (Cell Culture Facility, Duke University) were cultured in DMEM (Mediatech) supplemented with 10% fetal bovine serum (HyClone), 2.5 mM HEPES (Thermo-Fisher), and 1× non-essential amino acids (Thermo-Fisher) at 37 °C with 5% CO_2.

Transfection of DENV2 RNA

DENV2 stocks were generated by electroporation of 5 µg in vitro transcribed DENV2 RNA into $4×10^6$ BHK-21 cells at 250 V and 950 µF (Gene Pulser Xcell system, Bio-Rad). Supernatants were harvested at 48 and 72 h post-electroporation and titer was determined by focus forming assay. BHK-21 cells seeded in 6-well plates were infected by incubation with virus at a

multiplicity of infection of 0.1 for 2 h in serum-free DMEM. At 4 h post-infection, cells were seeded into 96-well plates (for immunofluorescence assay) or 6-well plates (for focus forming assay and RNA extraction). For transfection-based replication assays, BHK-21 cells cultured in 6-well plates were transfected with 2 µg of in vitro transcribed DENV2 RNAs using the *Trans*IT-mRNA transfection kit (Mirus Bio) according to the manufacturer's instructions. At 4 h post-transfection, cells were seeded into 96-well plates (for immunofluorescence assay) or 6-well plates (for focus forming assay and RNA extraction) for each time point. Sequences of mutant viruses were confirmed by sequencing of gene-specific amplicons, and the NS2A^{mut} and Env^{mut} viruses did not revert after 61 days of passage.

Focus forming assay for DENV2 titer

Serial dilutions of supernatants were used to infect Vero cells in triplicate wells of a 48-well plate. At 2 h post-infection, cells were overlaid with methylcellulose. At 72 h post-infection, cells were washed with PBS, fixed with 1:1 methanol/acetone, and immunostained with anti-Flavivirus Envelope 4G2 antibody (1:500 in 5% milk; gift of Dr. Mariano Garcia-Blanco, UTMB). Following binding of horseradish peroxidase-conjugated secondary antibody (1:1000 in 5% milk; Jackson ImmunoResearch), infected foci were visualized (VIP Peroxidase Substrate kit, Vector Laboratories) and were counted at 40× magnification to determine titer (in focus forming units per ml).

Quantification of DENV2 RNA by RT-qPCR

Intracellular RNA was extracted from cells (RNeasy mini columns, Qiagen). Extracellular RNA was isolated from cell supernatants of DENV2-infected cells (QIAamp Viral RNA kit, Qiagen). DENV2 RNA copy number was measured in triplicate by RT-qPCR (using the TaqMan Fast Virus 1-Step Mix, Thermo-Fisher) and a DENV2-specific primer-probe set (Applied Biosystems; Primers: S-ATTAGAGAGCAGATCTCTG, AS-GTCGACACGCGGTTTC, Probe-TCAATATGCTGAAACGCG). DENV2 copy number was calculated by comparison to a standard curve using in vitro transcribed DENV2 RNA.

Immunofluorescence assay

DENV2-infected or DENV2 RNA-transfected cells in 96-well plates were fixed in 4% paraformaldehyde and permeabilized with 0.2% Triton X-100. Cells were immunostained with anti-Flavivirus Envelope 4G2 antibody (1:1000) and AlexaFluor 488 conjugated secondary antibody (1:1000). Nuclei were stained with DAPI (1:1000). Cells were imaged (Cellomics

ArrayScan VTI HCS reader and associated software) to determine the percentage of DENV2-infected cells. At least 1000 cells were counted per well.

Data and software availability

All SHAPE data, associated standard errors, and RNA structure models are provided as supporting datasets and are also freely available at www.chem.unc.edu/rna. Custom software is also available from this website. Raw sequencing data for in virion and ex virion SHAPE-MaP and RING-MaP experiments are available from the Sequence Read Archive (SRP066015).

Recent related studies

The roles of RNA secondary structure in *Flaviviridae* replication are receiving increased interest, and multiple approaches are currently being taken to understand higher-order structures in hepatitis C, dengue and Zika viruses (32–36).

Supporting Information Acknowledgements

Dynamic light scattering experiments were performed in the UNC Macromolecular Interactions Facility (P30CA016086). Immunofluorescence assays were performed in the Duke Functional Genomics core facility.

Supporting Datasets

Dataset S1: SHAPE data

Table 1: Ex virion and in virion SHAPE reactivities

  --excel file with 1M7, 1M6, NMIA reactivities and associated standard errors

Table 2: Ex virion Shannon entropy

Table 3: Low SHAPE and Low Shannon entropy elements

  --includes beginning and ending nucleotide positions for all low SHAPE/Shannon regions

SHAPE-derived ex virion RNA model (.ct file)

Dataset S2: DMD data

Table 4: DMD models

  --includes beginning and ending nucleotide positions for models

  --includes DMD clustering results

Pymol sessions:

  --includes medoids and Theseus clusters for the 5'-UTR, Env, NS2A, NS2B, and 3'-UTR

Supporting Information References

1.   Liu Z-Y, et al. (2013) Novel cis-acting element within the capsid-coding region enhances flavivirus viral-RNA replication by regulating genome cyclization. *J Virol* 87(12):6804–18.

2.   Wilkinson KA, et al. (2008) High-throughput SHAPE analysis reveals structures in HIV-1 genomic RNA strongly conserved across distinct biological states. *PLoS Biol* 6(4):883–899.

3.   Watts JM, et al. (2009) Architecture and secondary structure of an entire HIV-1 RNA genome. *Nature* 460(7256):711–6.

4.   Deigan KE, Li TW, Mathews DH, Weeks KM (2009) Accurate SHAPE-directed RNA structure determination. *Proc Natl Acad Sci* 106(1):97–102.

5.   Siegfried NA, Busan S, Rice GM, Nelson JAE, Weeks KM (2014) RNA motif discovery by SHAPE and mutational profiling (SHAPE-MaP). *Nat Methods* 11(9):959–965.

6.   Rice GM, Leonard CW, Weeks KM (2014) RNA secondary structure modeling at consistent high accuracy using differential SHAPE. *RNA* 20(6):846–54.

7.   Williams R, et al. (2006) Amplification of complex gene libraries by emulsion PCR. *Nat Methods* 3(7):545–550.

8.   Smola MJ, Rice GM, Busan S, Siegfried NA, Weeks KM (2015) Selective 2'-hydroxyl acylation analyzed by primer extension and mutational profiling (SHAPE-MaP) for direct, versatile and accurate RNA structure analysis. *Nat Protoc* 10(11):1643–1669.

9.   Hajdin CE, et al. (2013) Accurate SHAPE-directed RNA secondary structure modeling, including pseudoknots. *Proc Natl Acad Sci U S A* 110(14):5498–503.

10.   Mathews DH (2004) Using an RNA secondary structure partition function to determine confidence in base pairs predicted by free energy minimization. *RNA* 10(8):1178–1190.

11.   Reuter JS, Mathews DH (2010) RNAstructure: Software for RNA secondary structure prediction and analysis. *BMC Bioinformatics* 11(1):129.

12.   Huynen M, Gutell R, Konings D (1997) Assessing the reliability of RNA folding using statistical mechanics. *J Mol Biol* 267(5):1104–1112.

13.   Smola MJ, Calabrese JM, Weeks KM (2015) Detection of RNA-Protein Interactions in Living Cells with SHAPE. *Biochemistry* 54(46):6867–6875.

14.   Homan PJ, et al. (2014) Single-molecule correlated chemical probing of RNA. *Proc Natl Acad Sci U S A* 111(38):13858–63.

15.   Rice GM (2015) High-throughput Experiment Driven Modeling of RNA Interactions and Structures.

16.   Yates F (1934) Contingency Tables Involving Small Numbers and the χ2 Test. *Suppl to J*

R Stat Soc 1(2):217.

17. Ding F, et al. (2008) Ab initio RNA folding by discrete molecular dynamics: From structure prediction to folding mechanisms. *RNA* 14(6):1164–1173.

18. Gherghe CM, Leonard CW, Ding F, Dokholyan N V., Weeks KM (2009) Native-like RNA tertiary structures using a sequence-encoded cleavage agent and refinement by discrete molecular dynamics. *J Am Chem Soc* 131(7):2541–2546.

19. Lavender CA, Ding F, Dokholyan N V., Weeks KM (2010) Robust and generic RNA modeling using inferred constraints: A structure for the hepatitis C virus IRES pseudoknot domain. *Biochemistry* 49(24):4931–4933.

20. Ding F, Lavender CA, Weeks KM, Dokholyan N V. (2012) Three-dimensional RNA structure refinement by hydroxyl radical probing. *Nat Methods* 9(6):603–608.

21. Barton GJ OC–A cluster analysis program.

22. Hajdin CE, Ding F, Dokholyan N V, Weeks KM (2010) On the significance of an RNA tertiary structure prediction On the significance of an RNA tertiary structure prediction. *RNA* 16(7):1340–1349.

23. Theobald DL, Wuttke DS (2008) Accurate structural correlations from maximum likelihood superpositions. *PLoS Comput Biol* 4(2).

24. DeLano WL (2002) The PyMOL Molecular Graphics System, Version 1.1. *Schrödinger LLC*:http://www.pymol.org.

25. Katoh K, Toh H (2008) Recent developments in the MAFFT multiple sequence alignment program. *Brief Bioinform* 9(4):286–298.

26. Muhire BM, et al. (2014) Evidence of Pervasive Biologically Functional Secondary Structures within the Genomes of Eukaryotic Single-Stranded DNA Viruses. *J Virol* 88(4):1972–1989.

27. Murrell B, et al. (2013) FUBAR: A fast, unconstrained bayesian AppRoximation for inferring selection. *Mol Biol Evol* 30(5):1196–1205.

28. Hasegawa M, Kishino H, Yano T aki (1985) Dating of the human-ape splitting by a molecular clock of mitochondrial DNA. *J Mol Evol* 22(2):160–174.

29. Muse S V. (1995) Evolutionary analyses of DNA sequences subject to constraints on secondary structure. *Genetics* 139(3):1429–1439.

30. Thurner C, Witwer C, Hofacker IL, Stadler PF (2004) Conserved RNA secondary structures in Flaviviridae genomes. *J Gen Virol* 85(5):1113–1124.

31. Kinney RM, et al. (1997) Construction of Infectious cDNA Clones for Dengue 2 Virus: Strain 16681 and Its Attenuated Vaccine Derivative, Strain PDK-53. *Virology* 230(2):300–

308.

32.   Mauger DM, et al. (2015) Functionally conserved architecture of hepatitis C virus RNA genomes. *Proc Natl Acad Sci U S A* 112(12):3692–3697.

33.   Pirakitikulr N, Kohlway A, Lindenbach BD, Pyle AM (2016) The Coding Region of the HCV Genome Contains a Network of Regulatory RNA Structures. *Mol Cell* 62(1):111–120.

34.   Huber RG, et al. (2018) Structure mapping of dengue and Zika viruses reveals new functional long- range interactions. *bioRxiv*. doi:10.1101/381368.

35.   Zhang QC, et al. (2018) Integrative analysis of Zika virus genome RNA structure reveals critical determinants of viral infectivity. *bioRxiv*. doi:10.1101/412577.

36.   Ziv O, et al. (2018) COMRADES determines in vivo RNA structures and interactions. *Nat Methods* 15(10):1.

37.   Brinton MA, Dispoto JH (1988) Sequence and secondary structure analysis of the 5′-terminal region of flavivirus genome RNA. *Virology* 162(2):290–299.

38.   Lodeiro MF, Filomatori C V, Gamarnik A V (2009) Structural and functional studies of the promoter element for dengue virus RNA replication. *J Virol* 83(2):993–1008.

39.   Polacek C, Foley JE, Harris E (2009) Conformational changes in the solution structure of the dengue virus 5' end in the presence and absence of the 3' untranslated region. *J Virol* 83(2):1161–6.

40.   Clyde K, Harris E (2006) RNA secondary structure in the coding region of dengue virus type 2 directs translation start codon selection and is required for viral replication. *J Virol* 80(5):2170–82.

41.   Groat-Carmona AM, et al. (2012) A novel coding-region RNA element modulates infectious dengue virus particle production in both mammalian and mosquito cells and regulates viral replication in Aedes aegypti mosquitoes. *Virology* 432(2):511–526.

42.   Olsthoorn RC, Bol JF (2001) Sequence comparison and secondary structure analysis of the 3' noncoding region of flavivirus genomes reveals multiple pseudoknots. *RNA* 7(10):1370–7.

43.   Pijlman GP, et al. (2008) A Highly Structured, Nuclease-Resistant, Noncoding RNA Produced by Flaviviruses Is Required for Pathogenicity. *Cell Host Microbe* 4(6):579–591.

44.   Manzano M, et al. (2011) Identification of cis-acting elements in the 3′-untranslated region of the dengue virus type 2 RNA that modulate translation and replication. *J Biol Chem* 286(25):22521–22534.

45.   Zeng L, Falgout B, Markoff L (1998) Identification of specific nucleotide sequences within

the conserved 3'-SL in the dengue type 2 virus genome required for replication. *J Virol* 72(9):7510–22.

46. Chapman EG, Moon SL, Wilusz J, Kieft JS (2014) RNA structures that resist degradation by Xrn1 produce a pathogenic Dengue virus RNA. *Elife* 3:e01892.

47. Sztuba-Solinska J, et al. (2013) Structural complexity of Dengue virus untranslated regions: Cis-acting RNA motifs and pseudoknot interactions modulating functionality of the viral genome. *Nucleic Acids Res* 41(9):5075–5089.

48. Villordo SM, et al. (2015) Dengue Virus RNA Structure Specialization Facilitates Host Adaptation. *PLOS Pathog* 11(1):e1004604.

49. Shurtleff a C, et al. (2001) Genetic variation in the 3' non-coding region of dengue viruses. *Virology* 281(1):75–87.

50. Chapman EG, et al. (2014) The structural basis of pathogenic subgenomic flavivirus RNA (sfRNA) production. *Science (80-)* 344(6181):307–310.

51. Akiyama BM, et al. (2016) Zika virus produces noncoding RNAs using a multi-pseudoknot structure that confounds a cellular exonuclease. *Science* 354(6316):1148–1152.

52. Selisko B, Wang C, Harris E, Canard B (2014) Regulation of Flavivirus RNA synthesis and replication. *Curr Opin Virol* 9:74–83.

53. Ward AM, et al. (2011) Quantitative mass spectrometry of DENV-2 RNA-interacting proteins reveals that the DEAD-box RNA helicase DDX6 binds the DB1 and DB2 3??? UTR structures. *RNA Biol* 8(6).

54. Alvarez DE, et al. (2005) Long-Range RNA-RNA Interactions Circularize the Dengue Virus Genome Long-Range RNA-RNA Interactions Circularize the Dengue Virus Genome. *J Virol* 79(11):6631–6643.

55. Friebe P, Shi P-Y, Harris E (2011) The 5' and 3' Downstream AUG Region Elements Are Required for Mosquito-Borne Flavivirus RNA Replication. *J Virol* 85(4):1900–1905.

56. Hahn CS, et al. (1987) Conserved elements in the 3′ untranslated region of flavivirus RNAs and potential cyclization sequences. *J Mol Biol* 198(1):33–41.

57. Gebhard LG, Filomatori C V., Gamarnik A V. (2011) Functional RNA elements in the dengue virus genome. *Viruses* 3(9):1739–1756.

58. Villordo SM, Carballeda JM, Filomatori C V., Gamarnik A V. (2016) RNA Structure Duplications and Flavivirus Host Adaptation. *Trends Microbiol* 24(4):270–283.

59. Kazantsev A V, Krivenko AA, Pace NR (2009) Mapping metal-binding sites in the catalytic domain of bacterial RNase P RNA. *RNA* 15(2):266–76.
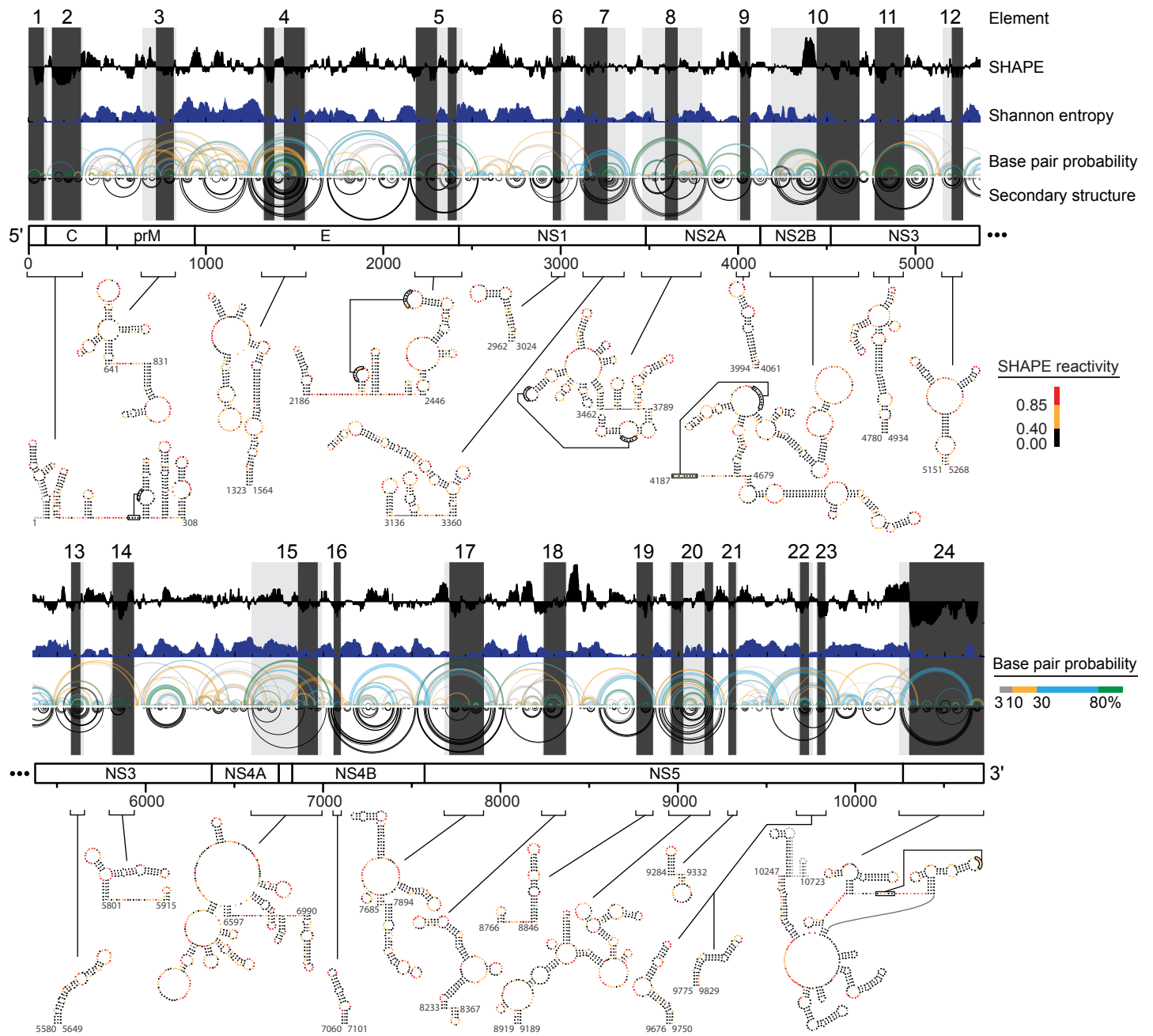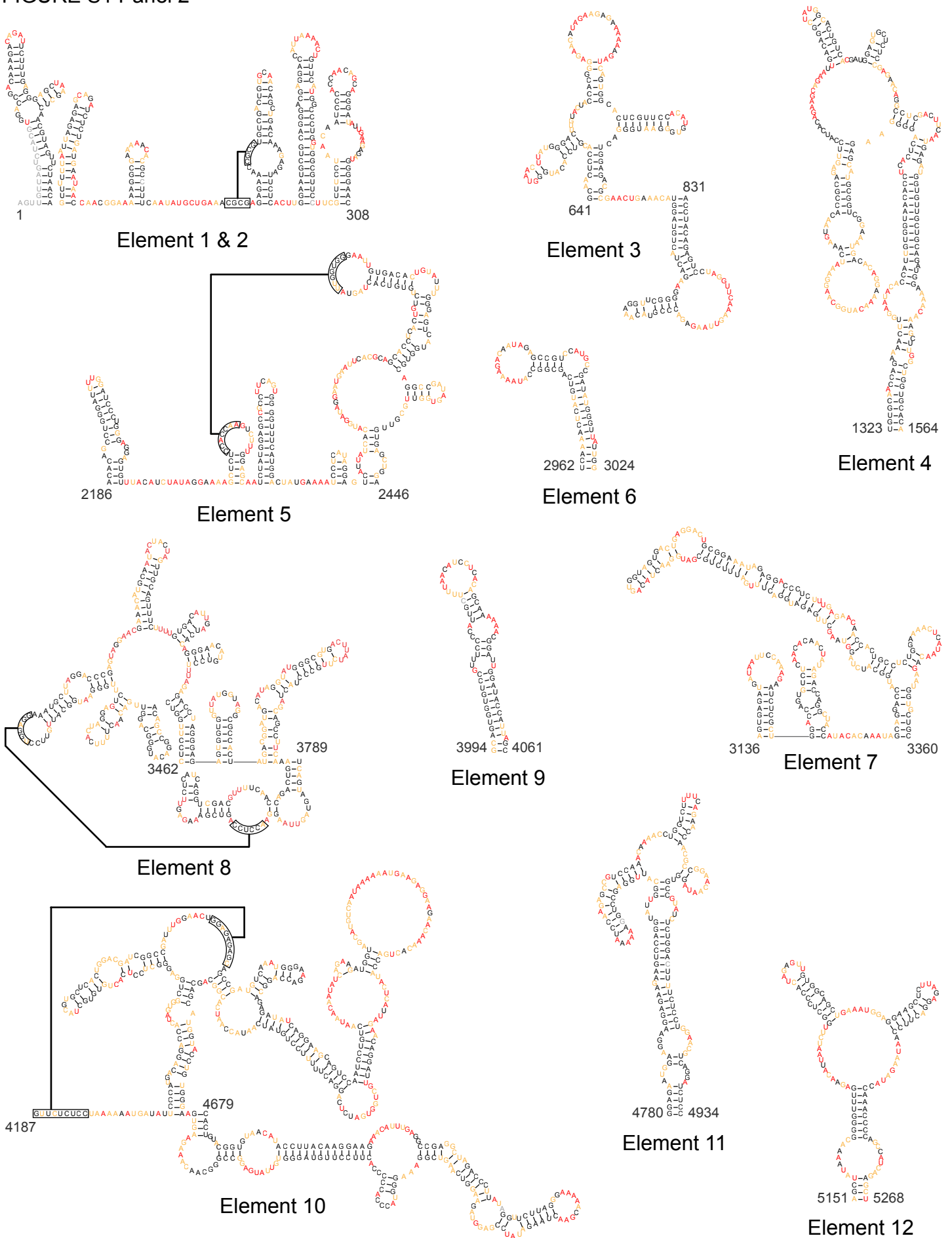
FIGURE S1 Panel 1

FIGURE S1 Panel 2

Element 1 & 2
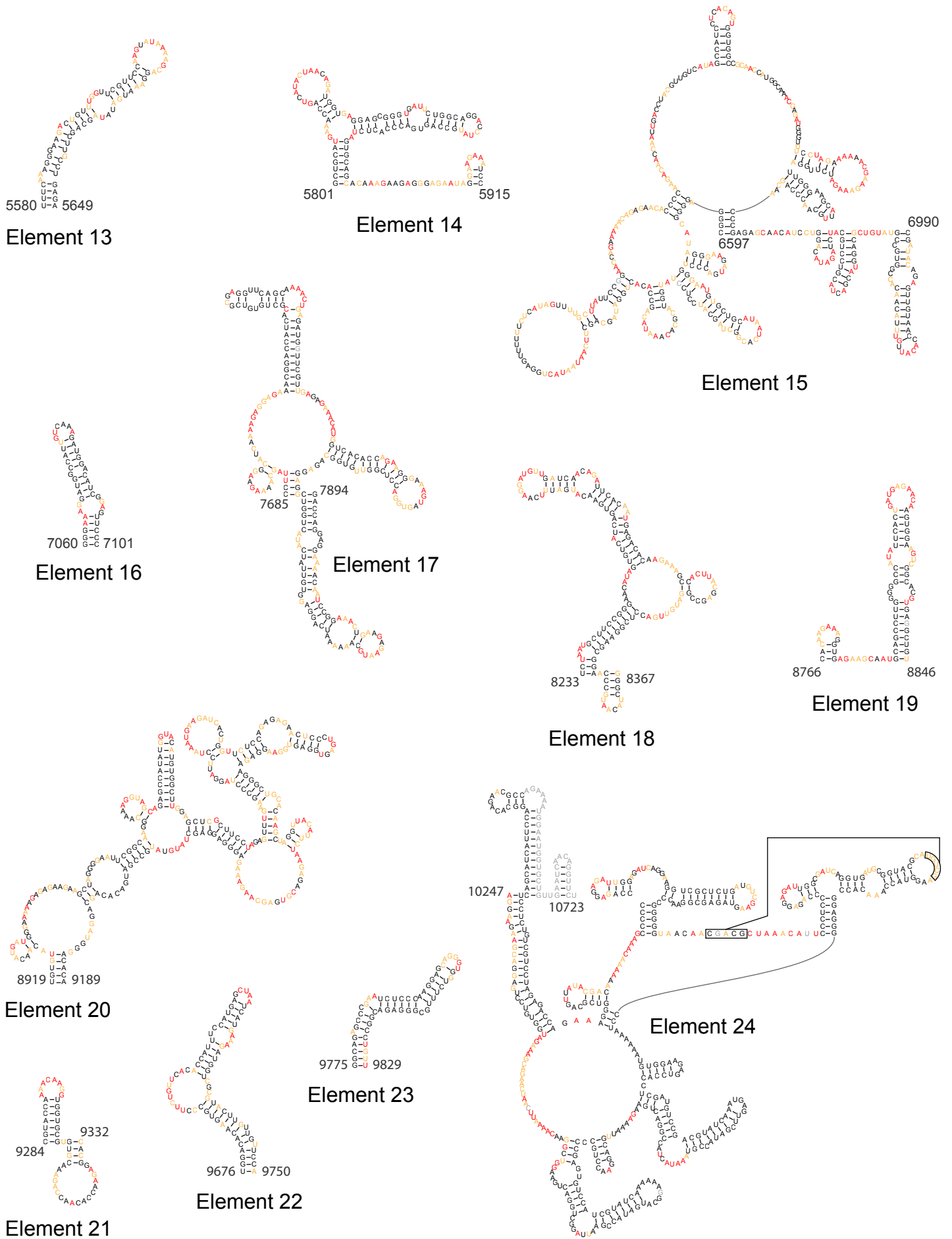
Element 3

Element 4

Element 5

Element 6

Element 8

Element 9

Element 7

Element 10

Element 11

Element 12

FIGURE S1 Panel 3

Element 13

Element 14

Element 15

Element 16

Element 17

Element 18

Element 19

Element 20

Element 21

Element 22

Element 23

Element 24

Figure S1: Well-determined secondary structure elements in the DENV2 RNA genome. (Panel 1) The entire genome is shown split into upper and lower panels (the first half of the genome, the upper panel, is also shown in Fig. 1). Median ex virion 1M7 SHAPE reactivities (black) and Shannon entropies (dark blue) are plotted over centered 55-nucleotide windows. Regions with both low SHAPE and low Shannon entropy are highlighted by dark-gray shading with light-gray shading extended to encompass entire intersecting helices. The 24 elements, with well-determined structures, are numbered. Base pair probability arcs are colored by probability (see scale), with green arcs indicating the most probable base pairs; black arcs indicate plausible pseudoknots (PK). The MFE secondary structure (inverted black arcs) was obtained using both 1M7 and differential SHAPE reactivities as constraints (6, 9). Secondary structures of all 24 elements are colored by SHAPE reactivity; high resolution structures are provided in panels 2 and 3 below. **(Panels 2 and 3)** Detailed secondary structures of all 24 elements with well-determined structures, from Figure 1 and panel 1 above, labelled with nucleotide identity, and colored by SHAPE reactivity.
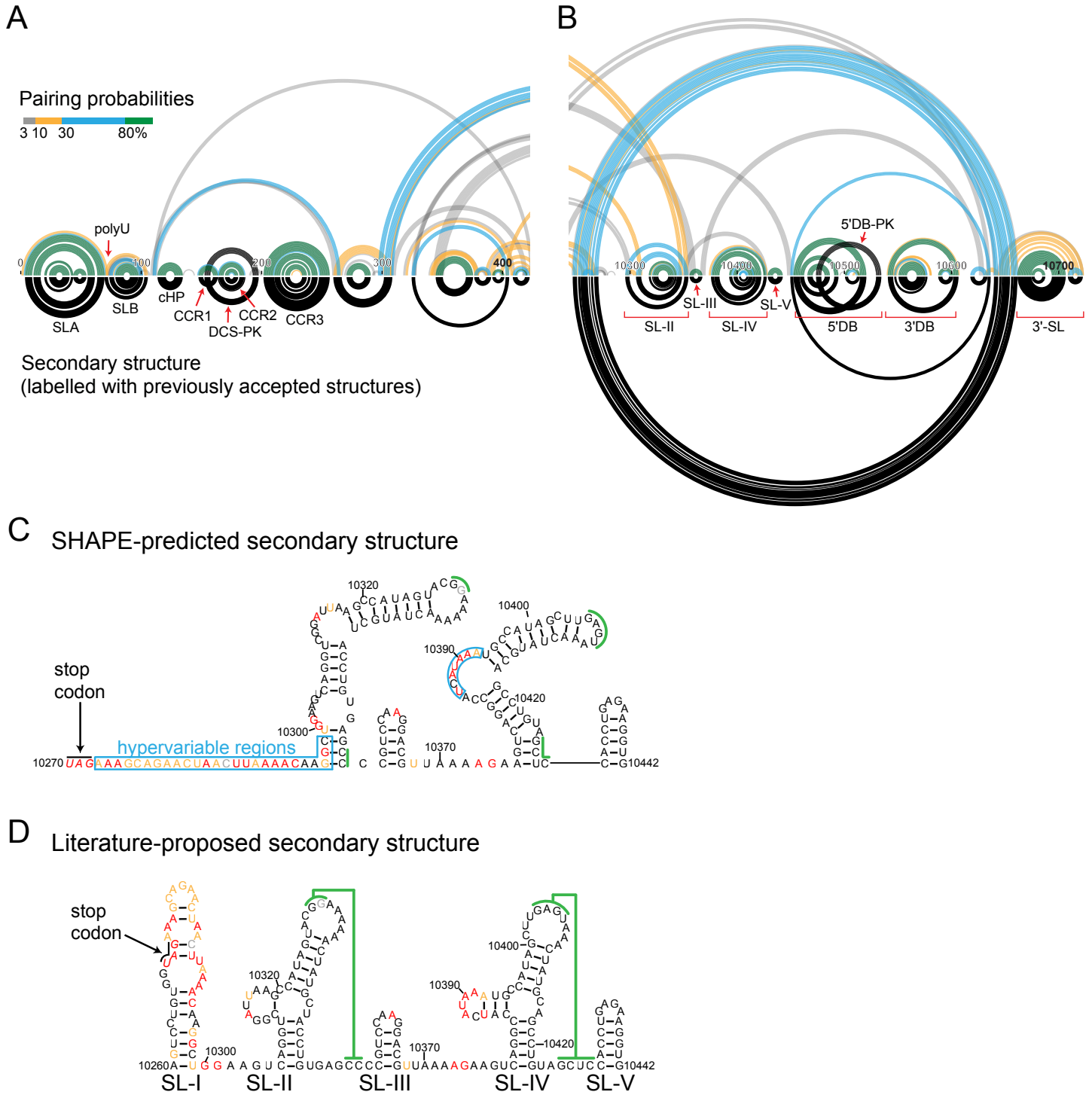
FIGURE S2

A

Secondary structure
(labelled with previously accepted structures)

B

C SHAPE-predicted secondary structure

D Literature-proposed secondary structure

Figure S2: Secondary structures of the 5'-UTR, capsid-coding region, and 3'-UTR. (**A**) SHAPE-directed MFE secondary structure of the 5'-UTR and a portion of the capsid-coding region is depicted by inverted black arcs below the line representing linear sequence. Above the line, colored arcs show base-pairing probabilities (see key), and black arcs indicate the DCS-PK pseudoknot. Known secondary structures (1, 32–36) are labeled. SLA, SLB, cHP, CCR1, CCR2, and CCR3 structures consist of highly probable base pairs (green). Other regions indicated by yellow, blue, and gray arcs are less probable. For example, the base pairs that involve the poly(U) stretch between SLA and SLB are less probable (yellow), as is the helix directly downstream of CCR3. (**B**) SHAPE-derived MFE secondary structure and base pair probability plot for the 3'-UTR. The black arcs in the pairing probabilities plot correspond to the 5'-DB-PK. Known secondary structures (37–40) are labeled. Most structures (SL-III, SL-IV, SL-V, 5'DB, 3'DB, and part of the 3'SL) are highly probable (green arcs). Our SHAPE data also supports the existence of the 5'DB pseudoknot characterized in previous studies (41–43). (**C**) SHAPE-derived secondary structure model for the variable region of the 3'-UTR. Nucleotides are colored by ex virion SHAPE reactivity. The hypervariable region is indicated by a blue box (44); SHAPE data shows this region to be highly flexible. Green lines indicate nucleotides of proposed pseudoknots (38, 41, 43). Recent crystal structures of an element in the Murray Valley encephalitis virus and Zika virus similar to SL-II and SL-IV revealed a highly compact structure with an additional pseudoknot (not shown) (45, 46). These three pseudoknots are supported by our SHAPE data although they were not predicted by our analysis, which requires a pseudoknot to span at least three base pairs. (**D**) Literature-proposed secondary structure of the variable region (38, 47, 48). Known structures are labeled, and proposed pseudoknots are indicated by green lines. Nucleotides are colored by ex virion SHAPE reactivity. Experimental SHAPE reactivities clearly disagree with the previously proposed SL-I structure but agree well with SL-II, SL-III, SL-IV, and SL-V models.
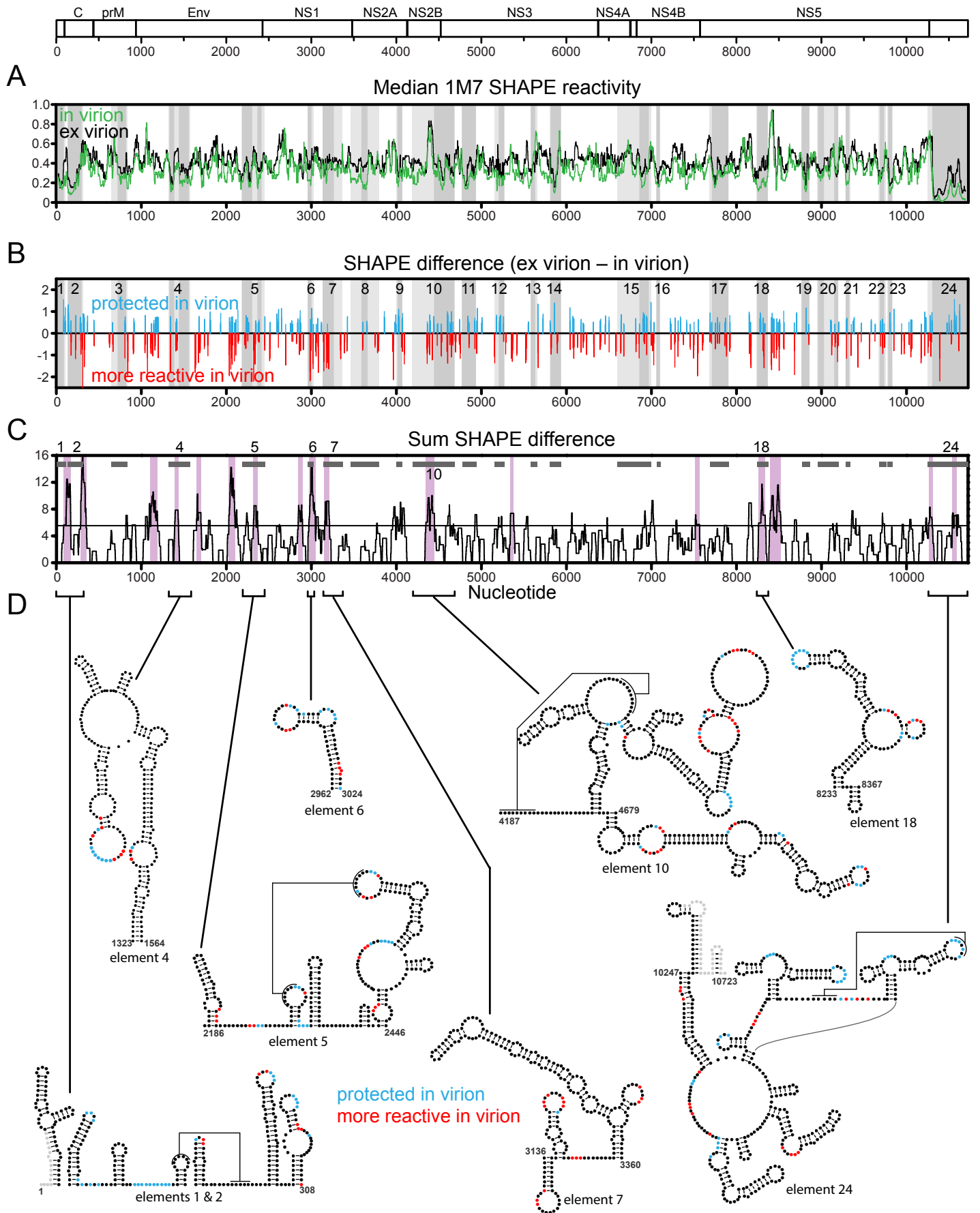
FIGURE S3

C | prM | Env | NS1 | NS2A | NS2B | NS3 | NS4A | NS4B | NS5

A — Median 1M7 SHAPE reactivity
in virion / ex virion

B — SHAPE difference (ex virion – in virion)
protected in virion
more reactive in virion

C — Sum SHAPE difference
Nucleotide

D
element 4
elements 1 & 2
element 6
element 5
element 7
element 10
element 18
element 24
protected in virion
more reactive in virion

Figure S3: Identification of nucleotides involved in structures that differ in virion versus ex virion. (**A**) Median ex virion and in virion SHAPE reactivities shown as centered 55-nucleotide windows in black and green, respectively. The 24 structural elements with low SHAPE reactivity and low entropy are indicated by gray boxes. (**B**) Significant differences between ex virion and in virion SHAPE reactivities. Blue and red bars indicate nucleotides that are protected or more reactive in virion than ex virion, respectively. (**C**) Sum of the absolute values of significant SHAPE differences over a 51-nucleotide window. The global median plus one standard deviation is indicated by a black line. Clusters of significant differences in SHAPE reactivity are highlighted by purple boxes. The 24 structural elements are indicated by gray boxes at the top of the plot. (**D**) Nine structural elements that contain clusters of significant differences between in virion and ex virion SHAPE data. Nucleotides are colored by SHAPE difference value.
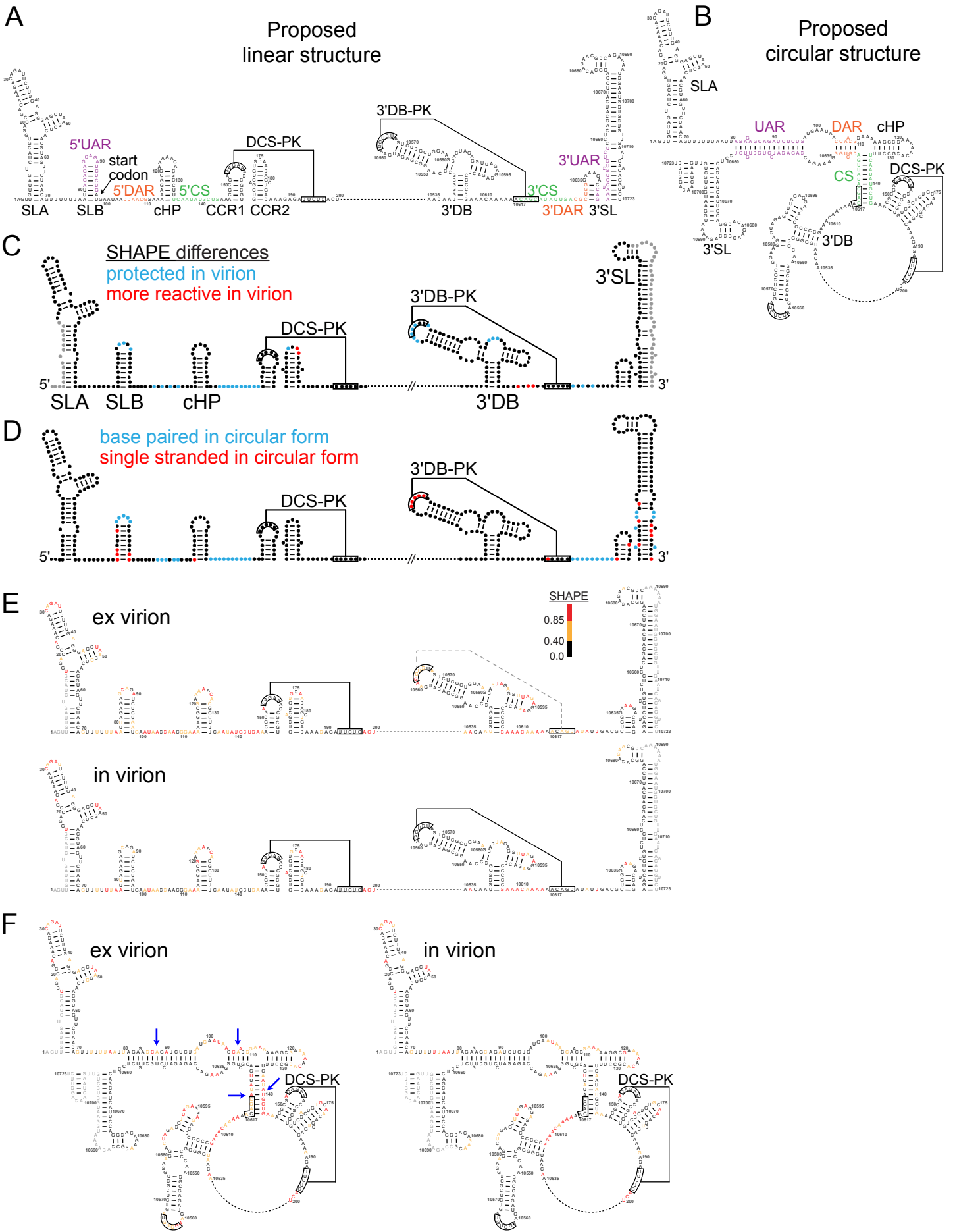
FIGURE S4

A   Proposed linear structure

B   Proposed circular structure

C   SHAPE differences
     protected in virion
     more reactive in virion

D   base paired in circular form
     single stranded in circular form

E   ex virion
     in virion

     SHAPE
     0.85
     0.40
     0.0

F   ex virion
     in virion

Figure S4: Linear and circular forms of the DENV2 genome. (**A**) Proposed secondary structures for the linear DENV2 genomic RNA. The dashed line represents the internal protein-coding region. Known structures are labeled. Pseudoknots DCS-PK and 3'DB-PK are shown. Nucleotides involved in long-range base pairs in the circularized form are indicated: 5' UAR and 3' UAR (purple) (49), 5' DAR and 3' DAR (orange) (50), 5' CS and 3' CS (green) (51). (**B**) Proposed secondary structures for the circular DENV2 genomic RNA. (**C**) Accepted secondary structure of the linear form of the 5'-UTR, capsid-coding region, and 3'-UTR with nucleotides colored by SHAPE *difference* value (47, 52, 53). (**D**) Nucleotides predicted to be base paired in the circular form but single stranded in the linear form are colored blue and those predicted to be single stranded in the circular form but base paired in the linear form are colored red. (**E**) Ex virion and in virion SHAPE reactivities superimposed on the proposed linear structure (see key). Positions with no data are in gray. The 3'DB-PK does not form in the ex virion RNA as indicated by a dashed gray line. (**F**) Ex virion and in virion SHAPE reactivities superimposed on the proposed circular structure. SHAPE reactivities that are incompatible with the circularized secondary structure model are highlighted with blue arrows.
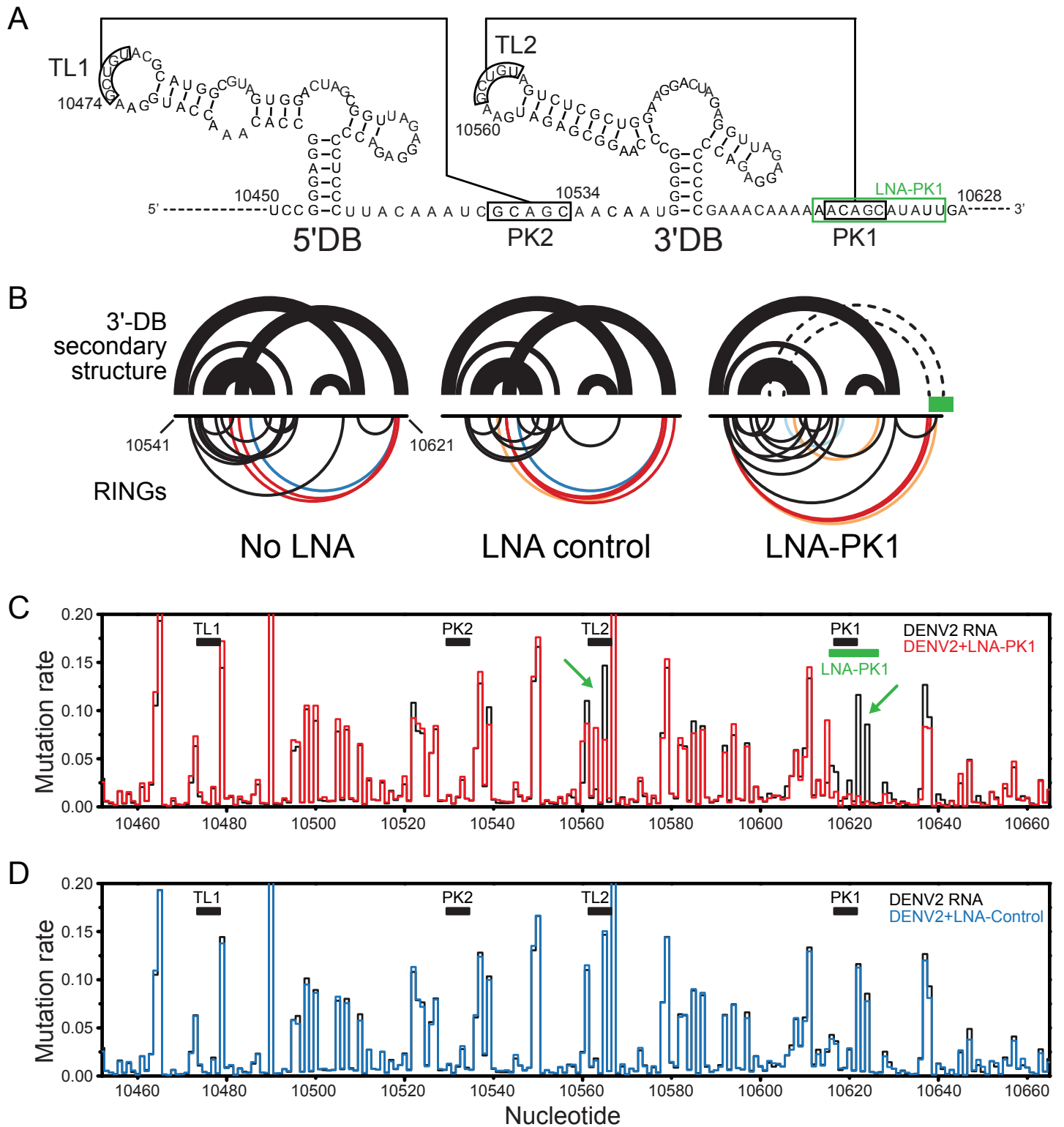
Figure S5: Effects of LNA binding on a tertiary RING-MaP experiment. (**A**) Secondary structures of the 5'DB and 3'DB motifs located in the 3'-UTR (37, 39). Nucleotides that form the 5'DB pseudoknot (TL1 and PK2) and the 3'DB pseudoknot (TL2 and PK1) are boxed and connected by lines. A green box highlights the predicted binding site for LNA-PK1. (**B**) Secondary structure arcs and RINGs obtained for the 3'-DB-PK in the absence and presence of an LNA control and LNA-PK1 oligonucleotide. The disrupted pseudoknot is shown with a dashed line. (**C**) DMS modification profiles in the RING-MaP experiment for the DENV2 RNA alone (black) and in the presence of LNA-PK1 (red). The locations of TL1, PK2, TL2, and PK1 nucleotides are indicated by black boxes. When DENV2 RNA was folded in the presence of LNA-PK1, DMS mutation rates at the predicted LNA binding site decreased, and there was a corresponding change in DMS mutation rate at TL2 (green arrows). These data indicate that LNA-PK1 binds to PK1 and inhibits formation of the 3'DB pseudoknot. (**D**) DMS modification profiles for the DENV2 RNA alone (black) and in the presence of a control LNA (LNA-Control, blue). No significant changes in DMS mutation rates were observed upon the addition of the LNA-Control.
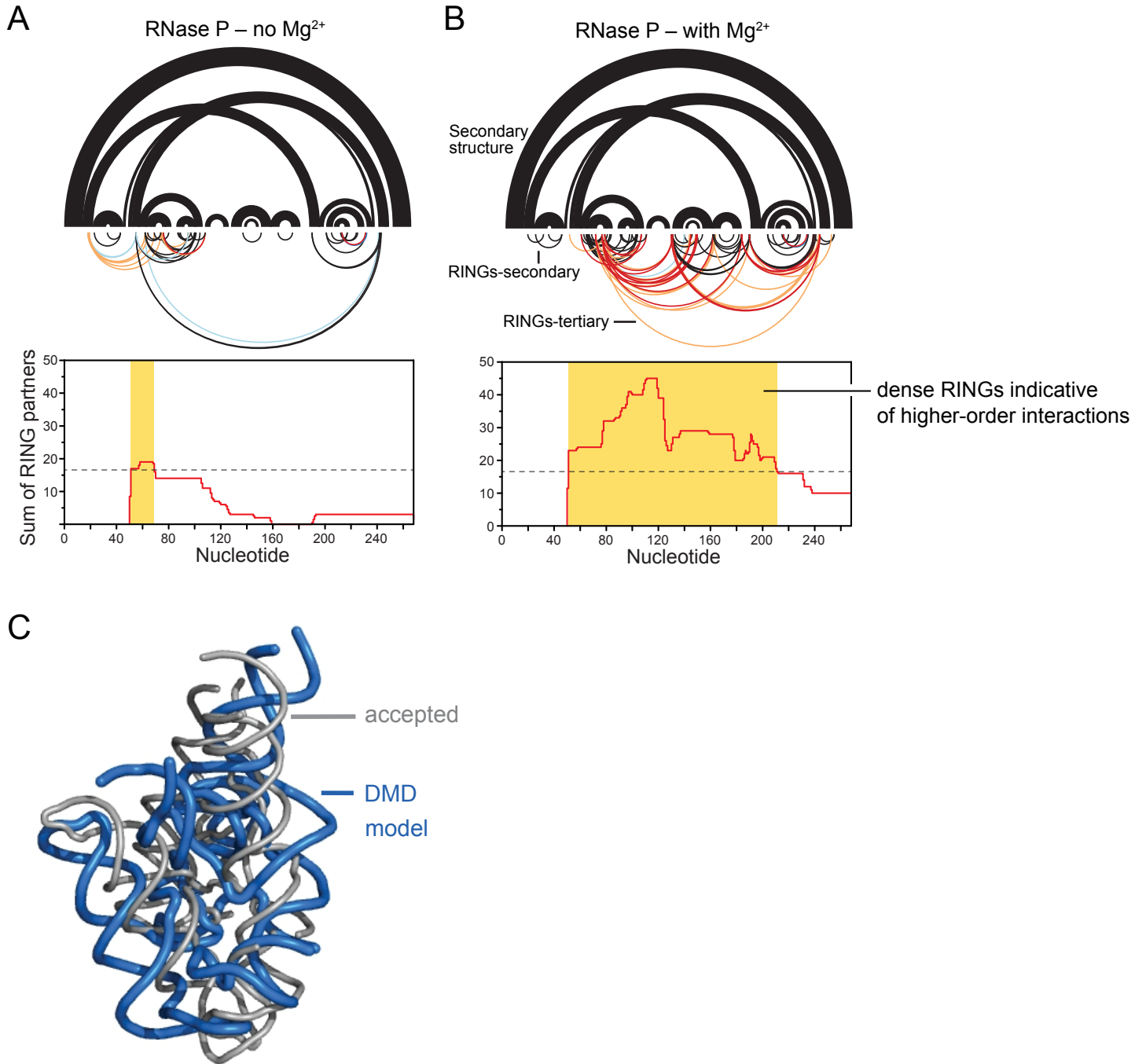
A

RNase P – no Mg²⁺

B

RNase P – with Mg²⁺

Secondary
structure

RINGs-secondary

RINGs-tertiary

dense RINGs indicative
of higher-order interactions

Sum of RING partners

Nucleotide

Nucleotide

C

accepted

DMD
model

Figure S6: Tertiary structure motif discovery using summed tertiary RINGs. (**A**, **B**) Upper panels show the secondary structure (black arcs), secondary structure RINGs (inverted black arcs), and tertiary structure RINGs (inverted colored arcs) for the RNase P RNA obtained in (**A**) the absence and (**B**) the presence of magnesium ions. Lower panels show tertiary RINGs summed over a 101-nucleotide window; positions with a RING density greater than the median plus one standard deviation are highlighted by yellow shading. (**C**) 3D model of the RNase P RNA obtained using RING restraints (14) compared to the accepted model (54) . RMSD is 22.4 Å.

FIGURE S7

sequence unique to p16681-T7G
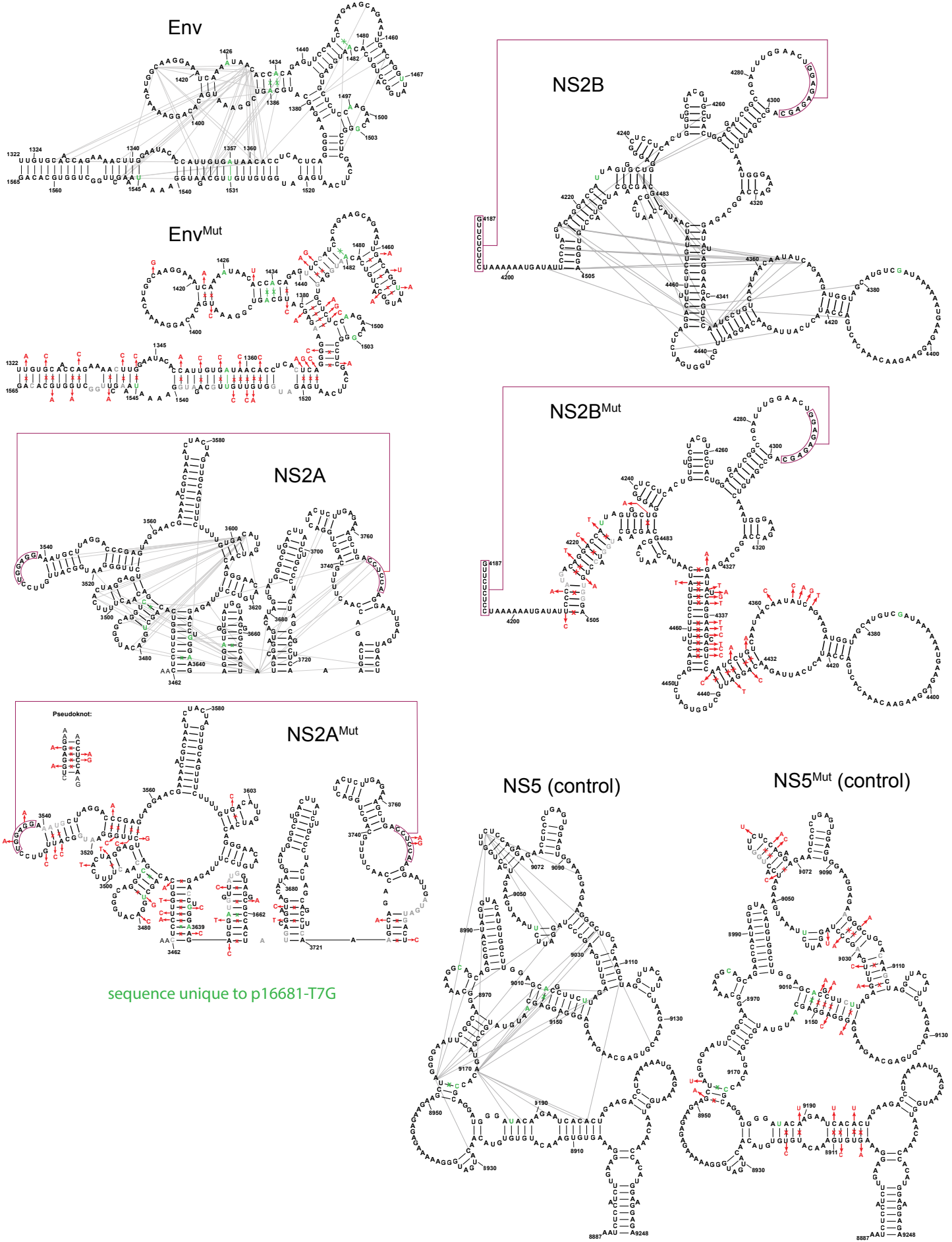
Figure S7: DENV2 mutants. Mutations in the Env, NS2A, NS2B and NS5 motifs designed to disrupt the ability of these regions to form tertiary interactions. Mutations were incorporated into full-length DENV2 clones. WT sequence (in the p16681-T7G clone) secondary structures are shown with tertiary RINGs illustrated as gray lines to emphasize rationale for mutating specific nucleotides and helices.
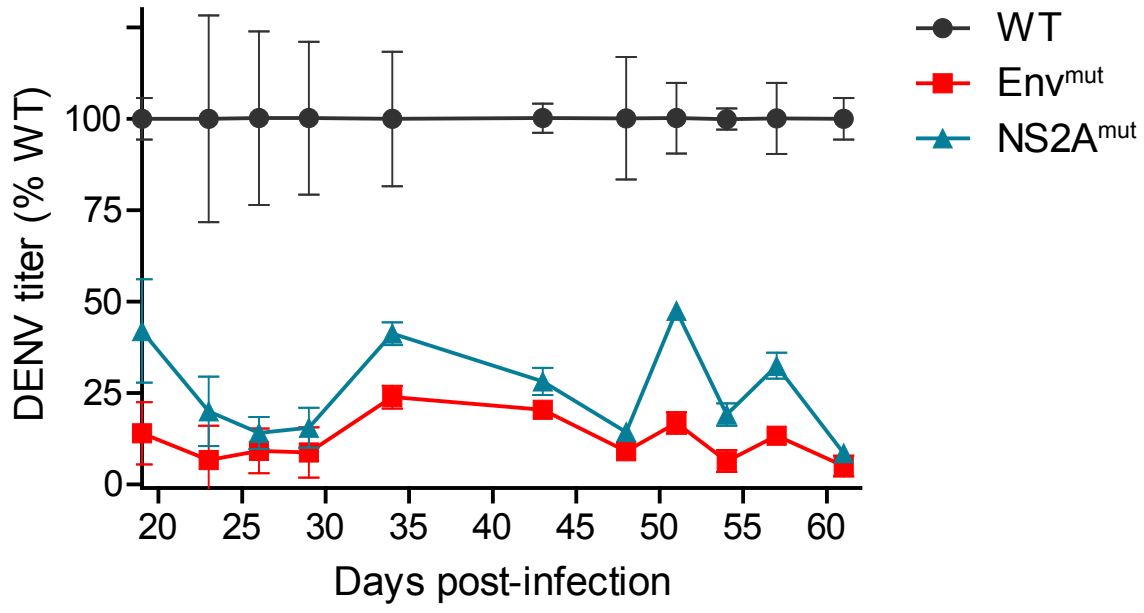
FIGURE S8

Figure S8: Reversion experiments. BHK-21 cells were infected with WT, Env^mut^, or NS2A^mut^ DENV2 stocks on Day 0 at an MOI of 0.003. Infected cells were serially passaged over the course of 61 days (16 passages), and virus particles in the supernatant were titered at each time point. There was no phenotypic reversion in the Env and NS2A mutants.
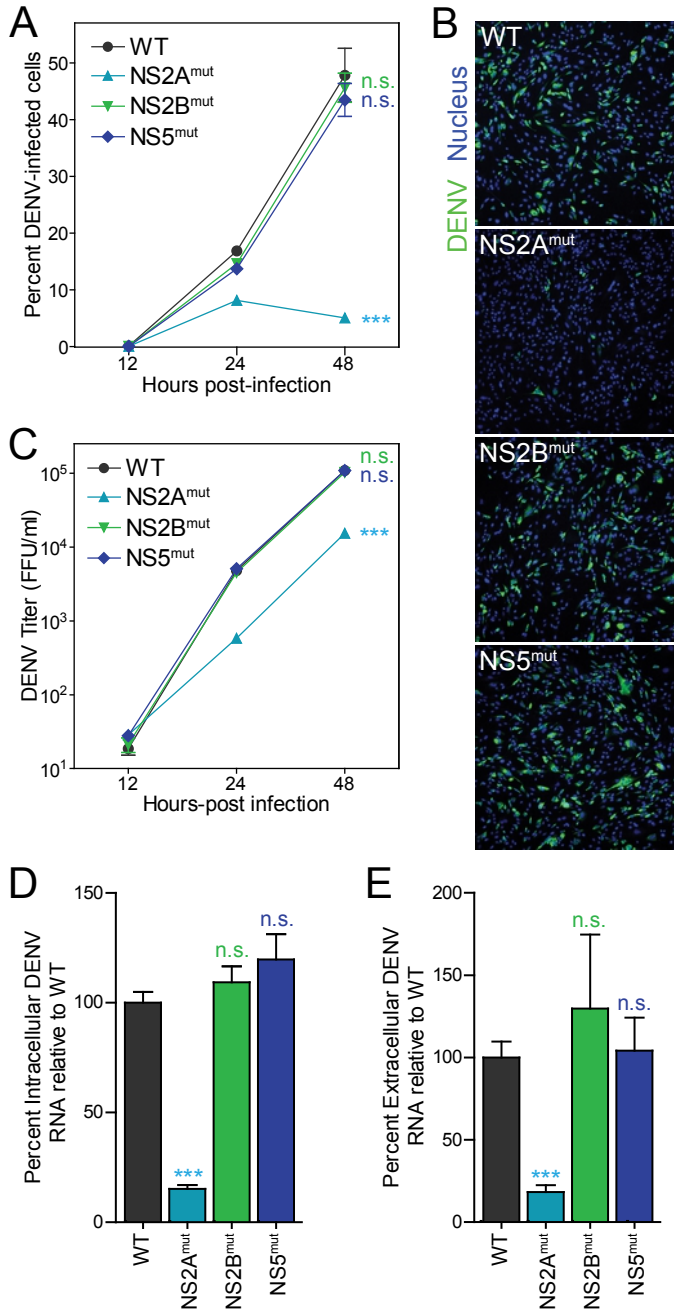
Figure S9: Full virus replication experiments. (**A**) Percentage of DENV2-positive BHK-21 cells over a time course after infection with WT or mutant DENV2 (multiplicity of infection 0.1) by immunostaining of DENV2 envelope protein and nuclei (n=4, with ≥1000 cells counted per condition. *** p≤0.001 by two-way ANOVA with Bonferroni correction). (**B**) Representative fields showing DENV2-infected cells (DENV, green), and nuclei (DAPI, blue) at 48 h post-infection from (A). (**C**) Viral titer, displayed as FFU/mL, following infection by WT or mutant DENV2 as determined by focus forming assay (n=3. *** p≤0.001 by two-way ANOVA with Bonferroni correction). (**D**) Percent of intracellular DENV2 RNA relative to WT in infected cells at 48 h post-infection as quantified by RT-qPCR (n=3, *** p≤0.001 by Student's t test). (**E**) Percent of intracellular DENV2 RNA relative to WT in infected cells at 48 h post-infection as quantified by RT-qPCR (n=3, *** p≤0.001 by Student's t test). Values represent the mean ± SEM of three independent experiments. n.s. = not significant.

FIGURE S10

Env^{mut2}

sequence unique to p16681-T7G

NS2A^{mut2}

Figure S10: Round-two DENV2 mutants. Env^{mut2} and NS2A^{mut2} mutants designed to selectively disrupt individual or adjacent nucleotides involved in RING correlations.
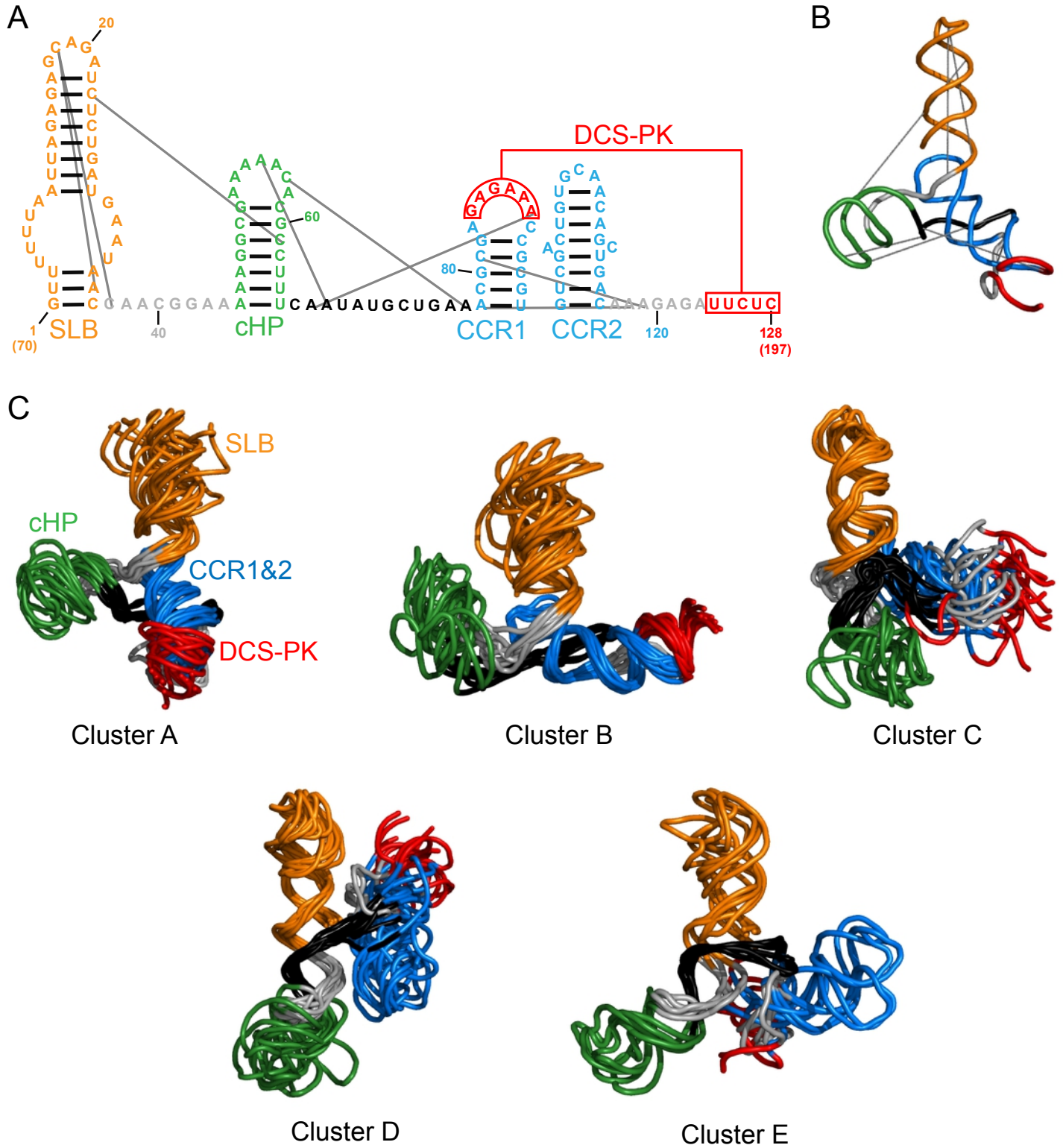
A

B

C

Cluster A

Cluster B

Cluster C

Cluster D

Cluster E

Figure S11: 5'-UTR element DMD 3D model. (**A**) Secondary structure model for part of the 5'-UTR and the capsid-coding region of DENV2 RNA (elements 1 and 2). RINGs used in the DMD simulation are shown with gray lines. The structure is numbered starting with the first nucleotide used in DMD modeling; nucleotide positions relative to absolute DENV2 genome location are shown in parentheses. Structures defined in prior work are labeled (47, 52, 53). (**B**) Medoid of the largest cluster A, with helices colored as shown in panel A. RINGs are depicted by gray lines. (**C**) The 10 lowest free-energy DMD models of clusters A (96 nodes), B (75 nodes), C (47 nodes), D (27 nodes), and E (5 nodes) were aligned using Theseus (23). In all clusters, CCR1 (blue) and CCR2 (blue) form a continuous helix. In cluster A, SLB (orange) is stacked on CCR1/2 domain (blue). In clusters C and D, SLB is stacked on cHP (green). The 3D structural diversity shown by these five clusters is due to the sparseness of RINGs in this region and suggests that there is no single, stable tertiary structure in this region.

FIGURE S12

A

B

C

D

E

Figure S12: Env element DMD 3D model. (**A**) Secondary structure of part of the envelope-coding region of DENV2 RNA (element 4). The structure is numbered starting with the first nucleotide used in DMD modeling; nucleotide positions relative to absolute DENV2 genome location are shown in parentheses. (**B**) The 10 lowest free-energy DMD models of cluster A (135 nodes). (**C**) Medoid of cluster A. (**D**) The 10 lowest free-energy DMD models of cluster B (115 nodes). (**E**) Medoid of cluster B.
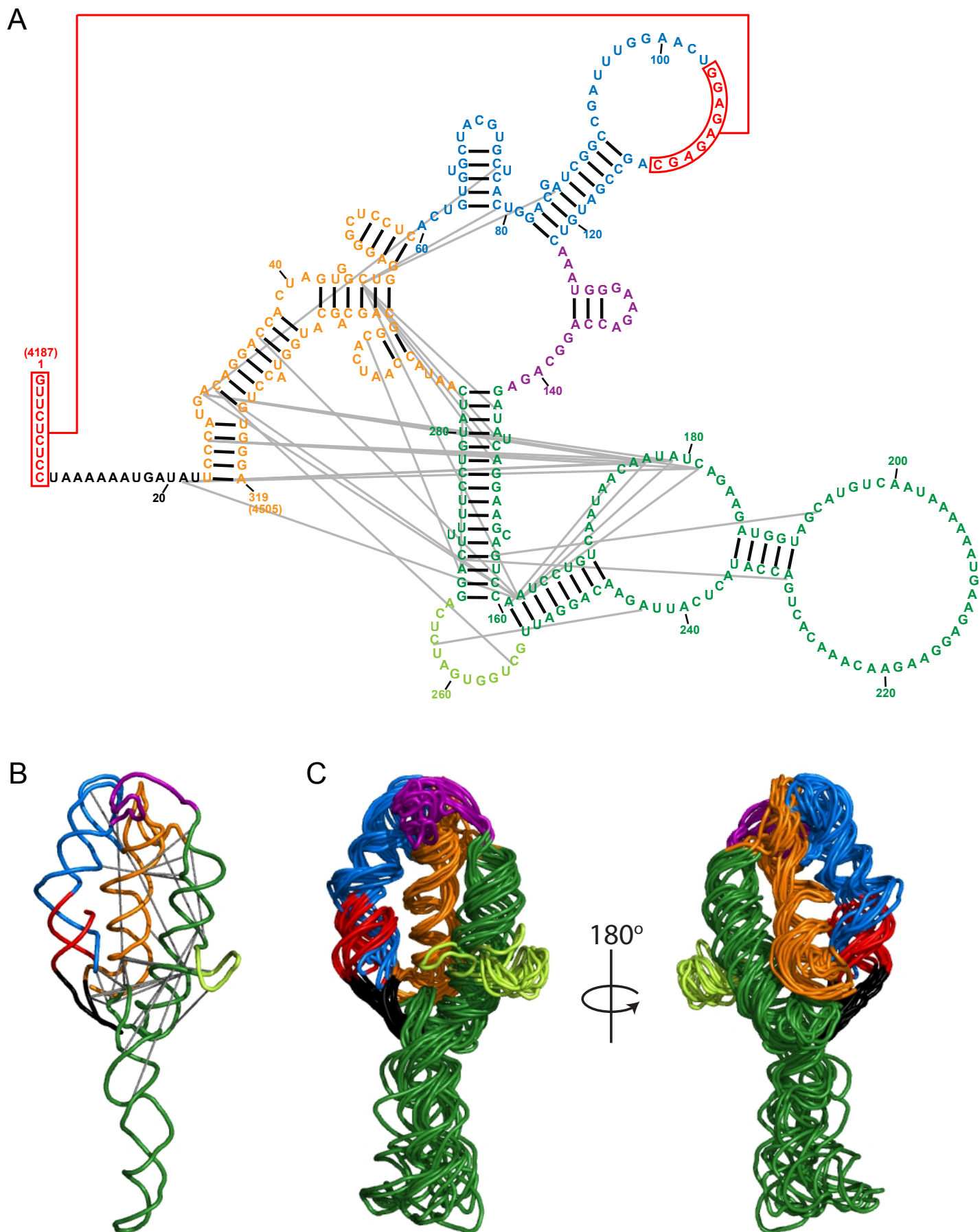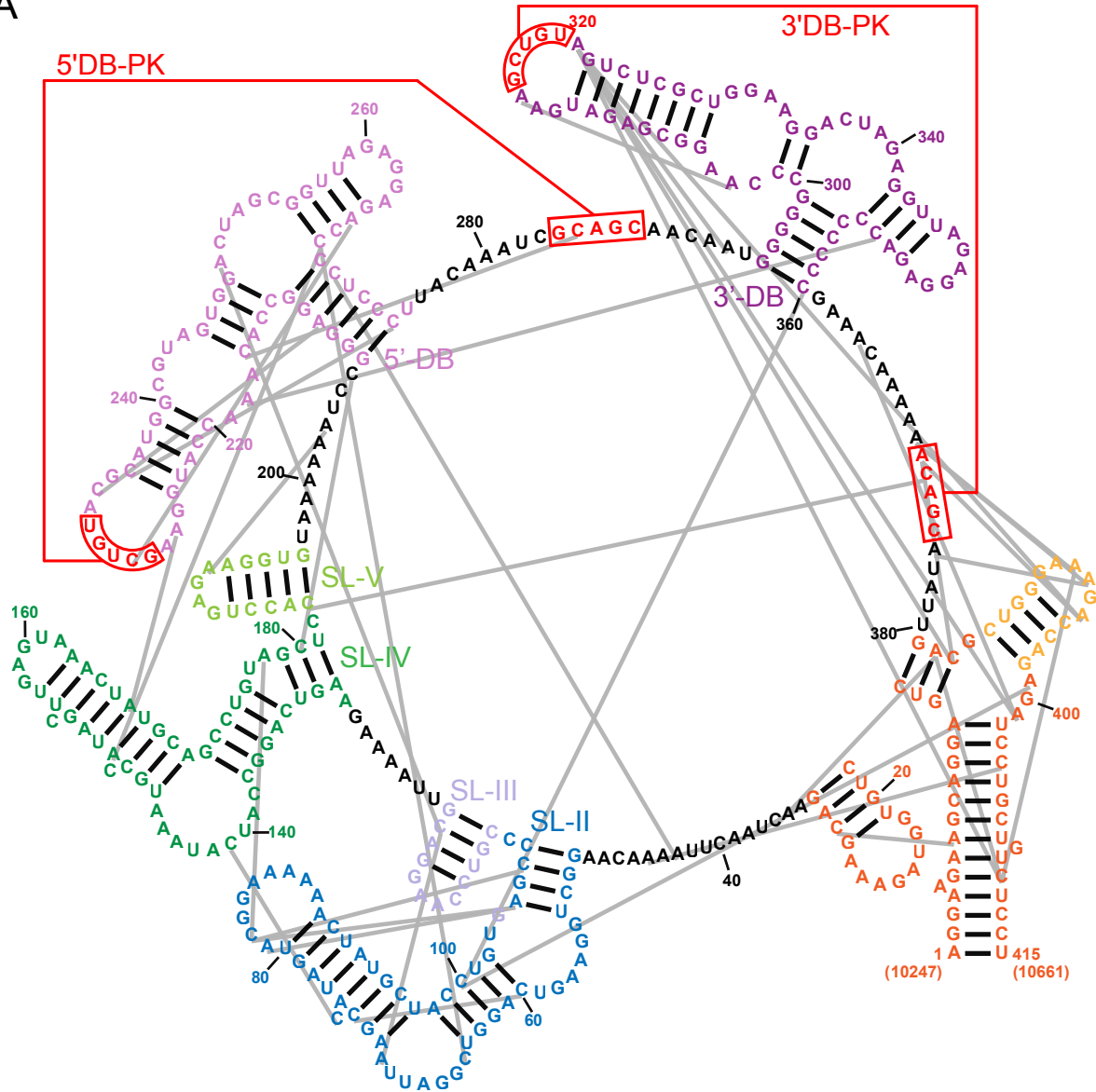
FIGURE S13

Figure S13: NS2B element DMD 3D model. (**A**) Secondary structure of the NS2B region of DENV2 RNA (element 10). The structure is numbered starting with the first nucleotide used in DMD modeling; nucleotide positions relative to absolute DENV2 genome location are shown in parentheses. (**B**) Medoid of cluster A. (**C**) The 10 lowest free-energy DMD models of cluster A (184 nodes).
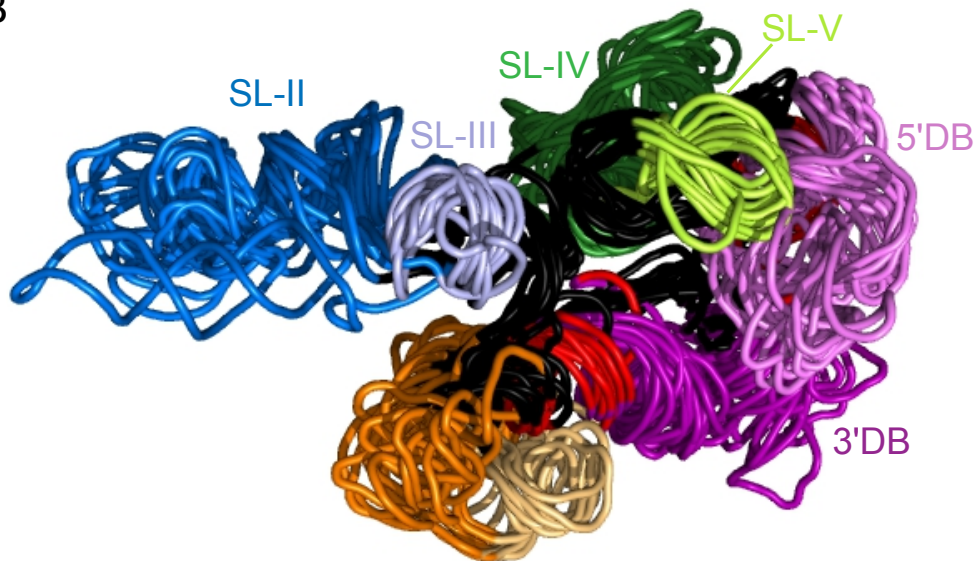
FIGURE S14

Figure S14: 3'-UTR element DMD 3D model. (**A**) Secondary structure of the 3'-UTR of DENV2 RNA (element 24). The structure is numbered starting with the first nucleotide used in DMD modeling; nucleotide positions relative to absolute DENV2 genome location are shown in parentheses. Known structures are labeled (37–40). (**C**) The 10 lowest free-energy DMD models of cluster A (151 nodes).